Synergistic use of Landsat 8 OLI image and airborne LiDAR data for above-ground biomass estimation in tropical lowland rainforests

Mui-How Phua [a*], Shazrul Azwan Johari [a], Ong Cieh Wong [a], Keiko Ioki [a], Maznah Mahali [a], Reuben Nilus [b], David A. Coomes [c], Colin R. Maycock [a], Mazlan Hashim [d]

[a] Mui-How Phua (pmh@ums.edu.my), Shazrul Azwan Johari (real_napster22@hotmail.com), Ong Cieh Wong (ciehwong@gmail.com), Keiko Ioki (keiko_ioki@ums.edu.my), Maznah Mahali (marz@ums.edu.my), Colin R. Maycock (colinr@ums.edu.my), Forestry Complex, Faculty of Science and Natural Resources, Universiti Malaysia Sabah, Sabah, Malaysia.

[b] Reuben Nilus (reuben.nilus@sabah.gov.my), Forest Research Centre, Sabah Forestry Department, P.O. Box 1407, 90715 Sandakan, Sabah, Malaysia

[c] David A. Coomes (david.coomes@gmail.com), Department of Plant Sciences, University of Cambridge, Downing Street, Cambridge CB2 3EA, UK

[d] Mazlan Hashim (mazlanhashim@utm.my), Research Institute of Sustainable Environment, Universiti Teknologi Malaysia, 91310 Skudai, Johor Bahru, Malaysia

[*] Corresponding author

Abstract

Developing a robust and cost-effective method for accurately estimating tropical forest's carbon pool over large area is a fundamental requirement for the implementation of Reducing Emissions from Deforestation and forest Degradation (REDD+). This study aims at examining the independent and combined use of airborne LiDAR and Landsat 8 Operational Land Imager (OLI) data to accurately estimate the above-ground biomass (AGB) of primary tropical rainforests in Sabah, Malaysia. Thirty field plots were established in three types of lowland rainforests: alluvial, sandstone hill and heath forests that represent a wide range of AGB density and stand structure. We derived the height percentile and laser penetration variables from the airborne LiDAR and calculated the vegetation indices, tasseled cap transformation values, and the texture measures from Landsat 8 OLI data. We found that there are moderate correlations between the AGB and laser penetration variables from airborne LiDAR data (r = -0.411 to -0.790). For Landsat 8 OLI data, the 6 vegetation indices and the 46 texture measures also significantly correlated with the AGB (r = 0.366 to 0.519). Stepwise multiple regression analysis was performed to establish the estimation models for independent and combined use of airborne LiDAR and Landsat 8 OLI data. The results showed that the model based on a combination of the two remote sensing data achieved the highest accuracy (R^2_{adj} = 0.81, RMSE = 17.36%) whereas the models using Landsat 8 OLI data airborne LiDAR data independently obtained the moderate accuracy (R^2_{adj} = 0.52, RMSE = 24.22% and R^2_{adj} = 0.63, RMSE = 25.25%, respectively). Our study indicated that texture measures from Landsat 8 OLI data provided useful information for AGB estimation and synergistic use of Landsat 8 OLI and airborne LiDAR data could improve the AGB estimation of primary tropical rainforest.

Keywords: Tropical forest; Above-ground biomass; Landsat 8 OLI; Airborne LiDAR; Borneo; REDD+

1. Introduction

Tropical rainforests are among the largest terrestrial carbon reservoirs, as well as supporting some of the highest levels of biodiversity (Brown and Lugo 1982; Huston and Marland 2003; Saatchi et al. 2011). Conserving these biodiversity and carbon-rich habitats through reduction of deforestation and forest degradation is seen as an effective mitigation measure to combat climate change and conserve biodiversity (Imai et al., 2014). Under the United Nations Framework Convention on Climate Change (UNFCCC), there are ongoing negotiations to develop a mechanism to reduce emissions from deforestation and forest degradation, through conservation, sustainable management of forests and enhancement of forest carbon stocks in developing countries (REDD+). Developing a robust and cost-effective method for accurately estimating carbon pool in tropical rainforests over large area is a fundamental requirement for the implementation of REDD+. Estimating above-ground biomass (AGB) is critical to quantify carbon stocks in the tropics since AGB of trees in tropical forests account for a significant part of the total carbon pool (Houghton et al., 2001).

AGB estimation in tropical forest involves field measurements which are time-consuming, costly and labor intensive. AGB estimation using remote sensing with field measurements is a cost-effective approach recommended for REDD+ (Stern 2007). To date, spaceborne optical and radar data as well as airborne Light Detection and Ranging (LiDAR) data have been employed and analyzed to develop AGB estimation models in different types of forests at various scales (Gibbs et al. 2007, Koch 2010). Several studies have demonstrated useful relationships between backscatters from spaceborne Synthetic Aperture Radar (SAR) data and AGB in tropical forests (Englhart et al. 2011, Morel et al. 2011, Saatchi et al. 2011), but it has been shown that the signal saturates at the high forest AGB, depending on wavelength (Balzter et al., 2007, Englhart et al., 2011, Mitchard et al., 2011). On the other hand, spaceborne optical data, especially Landsat data is probably the most frequently used medium spatial-resolution data in AGB estimation at local and regional scales (Sader et al. 1989, Roy and Ravan 1996, Nelson et al. 2000, Foody et al. 2003, Phua and Saito 2003, Lu 2005, Kelsey & Neff, 2014, Karlson et al. 2015). The advantages of medium resolution satellite data are the acquisition cost, revisiting frequency and the broad spatial coverage. However, a critical limitation of AGB estimation from Landsat data and other medium-to-coarse spatial resolution multispectral images is that the estimation is heavily affected by the spectral saturation in high biomass forests (Dube et al., 2014; Ingram et al., 2005; Lu, 2006; Mutanga et al., 2012; Mutanga and Skidmore, 2004; Nichol and Sarker, 2011). Therefore, vegetation-index based approaches have achieved only limited success in tropical and subtropical regions where the forests have high AGB, associated with complex structure and dense canopy, as well as high species diversity (Foody et al., 2001; Lu, 2005; Nelson et al., 2000).

Recent studies of AGB estimation suggest the usefulness of texture variables rather than spectral vegetation indices (Wijaya et al. 2010; Kelsey and Neff, 2014; Dube and Mutanga. 2015a). Several studies have used texture measures derived from high-resolution satellite data. These have shown that image textural measures have the potential to improve the characterization of different forest types (Eckert, 2012; Nichol and Sarker, 2011; Pandey et al., 2010; Pinto et al., 2012; Sarker and Nichol, 2011). Image texture variables could provide a promising opportunity for capturing forest structural attributes and may help improve AGB estimation in tropical forests by compensating for spectral saturation (Lu 2005; Kelsey and Neff 2014). Although there are several studies that have successfully used the texture variables of high-resolution satellite data to estimate AGB in tropical forests (Proisy et al., 2007; Ploton et al., 2012; Pargal et al., 2017), the relationship between the texture measures from medium spatial resolution sensors and AGB has not been studied fully, especially when compared to raw spectral band information and vegetation indices (Dube and Mutanga 2015a). More recently, Landsat 8 Operational Land Imager (OLI) data became available and it is assumed to provide better opportunities for understanding the contribution of forest ecosystems to the carbon cycle (Dube and Mutanga 2015b). Compared to Landsat 7 ETM+, the newly-launched Landsat 8 OLI sensor exhibits several design improvements, including narrower near infrared wavebands, higher signal-to-noise ratio, and enhanced radiometric sensitivity. Recent studies suggest that the image texture measures from Landsat 8 OLI data show good potential in estimating AGB in Sudano-Sahelian woodland (Karlson et al. 2015) and in African plantation forest (Dube and Mutanga 2015a). The challenging task for texture extraction in AGB estimation is how to identify suitable texture parameters together with the optimal window size (Lu 2005; Dube and Mutanga 2015a).

Although spectral information and texture measures derived from satellite images can be useful in AGB estimation, it does not capture the vertical height information of forest canopy. Forest canopy height is the 3-dimensional determinant of AGB of a forest (Asner et al. 2012b). Forest canopy height can be derived from active remote sensing systems (Brown, 2002; Lu, 2006; Mitchard et al., 2009). Several attempts have been made to estimate forest canopy height using synthetic aperture radar (SAR) (Köhler and Huth 2010, Saatchi et al. 2011b). The bistatic TanDEM-Xmission acquires multiple globally consistent single-pass interferometric datasets to create global digital elevation model (Krieger et al., 2007). Recent studies have attempted to estimate forest canopy height from the interferometric coherence analysis of the TanDEM-X mission data. However, it is likely that the inherent limitation of penetration into dense forest canopy still remains and therefore saturation problems at higher AGB level are expected (Kugler et al. 2014). Although, Minh et al. (2016) had improved AGB estimates for tropical forests in French Guiana using an airborne tomographic SAR approach.

Airborne LiDAR is widely recognized as a remote sensing technology that is capable of acquiring very accurate data on forest canopy and terrain height. LiDAR has been used successfully to estimate forest AGB in various regions including in the tropics without saturation problems (e.g., Zhao et al. 2009, Drake et al. 2003, Asner et al. 2012b, Ioki et al. 2014, Phua et al. 2016). Although airborne LiDAR data can provide highly accurate AGB estimation, it is possible that inclusion of an additional independent source of data that correlates with forest structure or other biophysical properties can further improve its ability to estimate AGB. Several studies have investigated the combined use of airborne LiDAR data and multispectral remotely sensed data for estimating AGB and other forest biophysical properties in boreal or temperate forests (Popescu et al. 2004, Hyde et al. 2006, Takahashi et al. 2010; Dalponte and Coomes 2016). However, the performance of the integrated use of the airborne LiDAR and Landsat 8 OLI data for AGB estimation has yet to be examined in tropical forests. Considering the ability of the image texture measures from Landsat 5 and Landsat 7 images, synergistic use of airborne LiDAR and multispectral satellite data for estimating AGB deserves further attentions. This study aims to examine the independent and combined use of airborne LiDAR and the widely-available Landsat 8 OLI data to accurately estimate the AGB of tropical lowland rainforests in the Sepilok Forest Reserve (SFR), Sabah, Malaysia. SFR is a protection forest reserve that contains three distinctive types of lowland tropical forests: alluvial, sandstone hill and heath forests that represent a wide range of AGB density and stand structure (Nilus et al. 2011). Therefore, it provides an attractive opportunity to evaluate the performance of the derived variables from each remote sensing data across different types of tropical lowland rainforests.

2. Materials and Methods

2.1 Study Area

The study area, SFR, is located at Sandakan, Sabah (5˚ 10’ N, 117˚56’ E). SFR is a primary lowland tropical forest of 4,924 ha in area under the protection of the Sabah Forestry Department. Sandakan receives an average annual rainfall of about 2400 mm throughout the year and has a mean annual temperature of 27.3˚C (Malaysia Meteorological Service Monthly Report, unpublished data).

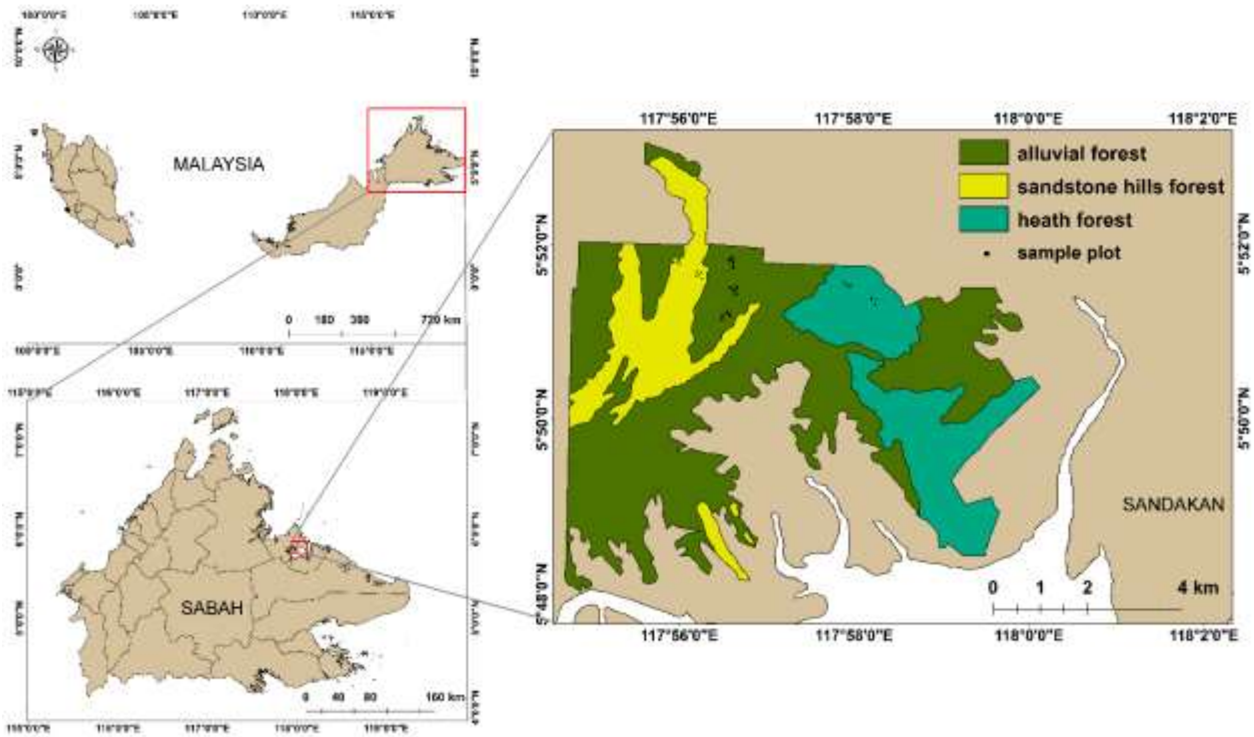

Fig. 1. Location of Sepilok Forest Reserve.

The SFR consists of three different forest types: alluvial, sandstone hill and heath (Kerangas) forests (Fox 1973). The Alluvial forest is dominated by large dipterocarp trees: the most abundant species in this forest type include *Parashorea tomentella* and *Shorea johorensis*. For the sandstone hill forest, the most abundant tree species are *Shorea multiflora*, *Shorea beccariana* and *Dipterocarpus acutangulus*. The heath forest is dominated by *Tristaniopsis merguensis* (Nilus et al. 2011).

2.2 Field Data Collection

A total of 30 plots were established within SFR from May 2013 to May 2015. Plot size varied according to differences in tree height within the different forest types. We established 50 m × 50 m plots in the alluvial forest and 30 m × 30 m plots in the heath and sandstone hill forests. Within the plots, the diameter at breast height (DBH) and tree height were measured for all trees having a DBH greater than 10 cm. Crown diameter were recorded only for 10 alluvial, 3 heath, 3 sandstone hill forest plots. The plot coordinates were determined by post-processing of differential GNSS (DGNSS) data using Javad Triumph-1 (JAVAD GNSS, San Jose, CA, USA). Of the 30 plots, 12 plots were located within the alluvial forest, 9 plots in the sandstone hill forest and 9 plots in the heath forest. All trees were identified to species level by local botanical experts. For the trees that could not be identified in situ, voucher specimens were collected and taken to the local herbarium. Samples that could not be identified to species were listed as morphospecies.

AGB was calculated according to the allometric equation of Chave et al. (2014) as:

$$AGB = 0.0673 \times (\rho \times D^2 \times H)^{0.976}$$

where D is DBH (cm), H is height (m) and ρ is the wood-specific gravity (g/cm^3). The wood-specific gravity ρ for the sampled species/genera were obtained from various sources (Lemmens et al., 1995; Soerianegara and Lemmens, 1993; Sosef et al., 1998). When a range of ρ values were reported for a species, a median value was used (Imai et al., 2014; Slik, 2006). In cases, where ρ values were unavailable for a species, the average across all species in that genus was applied (see Baker et al., 2004; Slik, 2006). When trees could not be identified at the generic level or where no literature record was available, the mean wood density of that plot was used. The summary of field measurements and crown measurements are presented in Table 1a and 1b, respectively.

Table 1a

Summary for the mean values of field measurements in each forest type.

Forest types	Height (m)	Lorey's height (m) [1]	DBH (cm)	AGB (t/ha)	Basal area (m^2/ha)	Wood density (g/cm^3) [1]
Alluvial forest	20.04	43.76	25.23	721.39	41.86	7.12
Heath forest	19.78	24.08	21.25	339.78	32.16	16.33
Sandstone hill forest	22.93	35.11	25.34	814.16	56.59	8.38
All forests	20.83	35.26	24.07	646.06	43.37	10.26

[1] Weighted by basal area

Table 1b

Crown diameter measurements from the 10 alluvial, 3 heath, and 3 sandstone hill forest plots.

Forest types	Alluvial forest	Heath forest	Sandstone hill forest	All forests
Crown diameter (m)				
Max	30.48	14.80	20.85	30.48
Mean	4.80	6.26	6.90	6.81
Min	1.20	0.88	0.35	0.35
S.D.	3.97	1.97	3.41	3.44

2.3 Landsat 8 OLI image

We acquired a Landsat 8 OLI image of SFR (path 117, row 56) that was taken on 25 August 2014. The Landsat 8 OLI sensor provides multispectral data with a spatial resolution of 30 meters. For each of the six bands from the Landsat 8 OLI image, (Band 2-blue, 3-green, 4-

red, 5-near infrared, 6-SWIR1 and 7-SWIR2), we converted the digital number (DN) value to top of atmosphere (TOA) radiance for every pixel using the radiance rescaling factors in the attached metadata file. An atmospheric correction was conducted using the Dark Subtraction Method (Chavez 1988). Table 2 shows the vegetation indices computed from the Landsat data included in this study: Normalized Vegetation Difference index (NDVI), Transformed Vegetation Index (TVI), Simple Vegetation Index (SVI), Differenced Vegetation Index (DVI), Ratio Vegetation Index (RVI), Normalized Ratio Vegetation Index (NRVI) and Soil Adjusted Vegetation Index (SAVI). In addition, the tasseled cap transformation was applied to the Landsat data to produce brightness, greenness and wetness indices (Table 2).

Table 2

Selected vegetation indices and image texture measures derived from Landsat 8 OLI image.

Parameters	Equation	References
Vegetation indices		
Normalized vegetation difference index (NDVI)	(NIR - red) / (NIR + red) + 0.5	Rouse et al. (1974)
Transformed vegetation index (TVI)	$\sqrt{(\mathrm{NIR} - \mathrm{red}) / (\mathrm{NIR} + \mathrm{red}) + 0.5}$	Deering et al. (1975)
Simple vegetation index (SVI)	red / NIR	Tucker (1979)
Differenced vegetation index (DVI)	NIR - red	Tucker (1980)
Ratio vegetation index (RVI)	NIR / red	Jordan (1969)
Normalized ration vegetation index (NRVI)	(RVI - 1) / (RVI + 1)	Baret and Guyot (1991)
Soil adjusted vegetation index (SAVI)	{(NIR - red) / (NIR + red + 0.5)} x (1 + 0.5)	Heute (1988)
Tasseled cap transformation		
Brightness	0.3029B2 + 0.786493B3 + 0.4733B4 + 0.5599B5 + 0.508B6 + 0.1707B7	Huang et al. (2002)
Greenness	-0.2941B2 - 0.243B3 - 0.5424B4 -	Huang et al. (2002)

Wetness	0.7276B5 + 0.0731B6 - 0.1608B7 0.1511B2 + 0.1973B3 + 0.3283B4 + 0.3407B5 - 0.7117B6 - 0.4559B7	Huang et al. (2002)
Gray-level co-occurrence matrices (GLCM)		
Mean	$\sum_{ij=0}^{N-1} iP_{ij}$	
Variance	$\sum_{ij=0}^{N-1} P_{ij}(i-\mathrm{Mean})^2$	
Homogeneity	$\sum_{ij=0}^{N-1} P\frac{P_{ij}}{1+(i-j)^2}$	
Dissimilarity	$\sum_{ij=o}^{N-1} P_{ij}\lvert i-j\rvert$	
Entropy	$\sum_{ij=o}^{N-1} P_{ij}(-\ln P_{ij})$	
Second moment	$\sum_{ij=o}^{N-1} {P_{ij}}^2$	
Correlation	$\sum_{ij=o}^{N-1} P_{ij}\left[\frac{(i-\mathrm{Mean})-(j-\mathrm{Mean})}{\sqrt{\mathrm{Variance}_i \mathrm{Variance}_j}}\right]$	
Contrast	$\sum_{ij=0}^{N-1} P_{ij}(i-j)^2$	

Texture variables were derived using Gray-Level Co-occurrence Matrices (GLCM) texture algorithms calculated with a relative displacement vector (*d*, *Θ*), which explains the spatial distribution of the level pairs separated by *d* in direction *Θ* (Haralick et al., 1973). Based on the study of Lu (2005), we selected eight texture variables: mean, variance, homogeneity, dissimilarity, entropy, second moment, correlation and contrast as predictors (Table 2). The performance of texture variables in AGB estimation depends on the moving window size (Kelsey and Neff 2014). All texture variables were computed using the six Landsat 8 OLI multispectral bands with five moving window sizes: 3 × 3, 5 × 5, 7 × 7, 9 × 9, and 11 × 11 pixels.

2.4 Airborne LiDAR data

Airborne LiDAR data were acquired in October 2013 using an Optech Orion C200 sensor, mounted on a Nomad C22 aircraft. The LiDAR data was collected at an altitude of 600 m a.g.l, speed of 41.2 m/s, scan angle of ±14° and pulse density of 10.58 pulses per square meter. The sensor system also consists of a DGNSS receiver coupled to an inertial measurement unit, both components ensuring that a sub-decimeter differential position can be calculated for the aircraft in post-processing. A residential area less than 20 km from the SFR was also scanned for calibration of the LiDAR data.

The point clouds were calibrated with a root-mean-square error (RMSE) of 0.0028 m for the 9 flight lines. The processed LiDAR point clouds were separated into two different classes; ground and non-ground points. The ground points were triangulated using natural neighbor to generate a digital terrain model (DTM) raster in ArcGIS software. We calculated three canopy height models (CHMs) following Asner and Mascaro (2014). CHMs are calculated by subtracting the DTM value from the non-ground point's z value. The top canopy height (TCH) model was determined from the maximum z value of the points, while the mean and medium CHMs were calculated based on the mean (MeanCH) and median (MedCH) z values of the points. The laser penetration (LP) rates were calculated as the ratio of last of many returns below a certain height (1, 2, 5, 7, 10, 12, 14, 16, 18, 20 or 28 m) relative to the number of laser shots (i.e. sum of the number of first of many returns and single returns), giving twelve laser penetration variable LP1, LP2, LP5, LP7, LP10, LP12, LP14 LP16, LP18, LP20 and LP28:

$$\mathrm{LP}(x) = \frac{\text{Number of the last returns at height } (x) \text{ m}}{\text{Sum of number of the first returns and number of single returns at height } (x) \text{ m}}$$

Although the data included multiple returns from each shot, we used only the first and last returns for LP calculation (Ioki et al., 2014). These CHMs and LPs were computed at 1-m resolution and their average values were derived for each field plot. In addition, the 60th, 70th, 80th and 90th percentiles (h_{60}, h_{70}, h_{80}, and h_{90}) were also calculated from the height of point clouds for all the plots.

2.5 Statistical analysis

The correlations between field AGB and the computed variables from the Landsat 8 OLI and LiDAR data were examined using Pearson's correlation. AGB estimation models were then developed using stepwise multiple linear regression analysis. In order to examine the performance of each remotely sensed data product and their combination, we conducted the regression analysis with 1) only Landsat 8 OLI image variables, 2) only LiDAR variables, and 3) Landsat 8 OLI image variables and LiDAR variables. The variables were natural-log transformed because canopy heights are known to have nonlinear (i.e. multiplicative) relationship with other structural variables e.g. DBH and AGB (Yamakura et al. 1986; Basuki et al. 2009). Since we had a limited number of field plots, leave-one-out cross-validation was performed to avoid overfitting of the model. The performance of the estimation models was evaluated using adjusted coefficient of determination (R^2_{adj}), RMSE and RMSE from cross-validation results (noted as RMSEcv). The statistical analyses were carried out using SPSS Statistics 21 (IBM, USA). To examine multi-collinearity effects, variable inflator factor (VIF) was calculated. We considered a VIF value greater than 10 as unacceptable for multicollinearity (Zuur et al. 2010).

3. Results

3.1 Pearson correlation analysis

Statistically significant Person's correlation coefficient (*r*) for the relationship between AGB and derived variables from airborne LiDAR data and Landsat 8 OLI image are presented in Table 3. There were relatively strong negative correlations between the LiDAR LP variables and the field observed AGB, with the highest *r* of -0.790 for LP24. LiDAR height variables also had moderate correlations, which ranged between r = 0.480 – 0.614. For Landsat 8 OLI variables, 46 out of 200 variables from texture measures had moderate correlations: mean of band 3 (green), variance of band 4 (red), homogeneity of band 4 (red) and 5 (near-Infrared), contrast of band 4 (red), dissimilarity of band 4 (red), entropy of bands 4 (red) and 5 (near-Infrared), second moment of bands 4 (red) and 5 (near-Infrared), correlation of bands 4 (red) with different moving window sizes. The highest correlation coefficient value among texture measures was observed for the homogeneity of band 4 (red) with 3 × 3 moving window size, the correlation of band 4 (red) with 3 × 3 and 5 × 5 moving window size ($|r| = 0.519$), followed by the homogeneity of band 4 (red) with 7 × 7 and 11 × 11 moving window size ($r = -0.516$), the contrast of band 4 (red) with 7 × 7 and 11 × 11 moving window size ($r = 0.516$) and the dissimilarity of band 4 (red) with 9 × 9 moving window size ($r = 0.516$). Five out of the 6 vegetation indices had weak correlations, ranged between $|r| = 0.406 – 0.419$, however, none of the tasseled cap transformation values from Landsat 8 OLI image were significantly correlated with field observed AGB.

Table 3

Statistically significant Pearson's correlation coefficients *r* between the field observed AGB and the derived variables from airborne LiDAR data and Landsat 8 OLI image.

Variables	*r*		Variables	*r*	
LiDAR height variables			*Landsat 8 OLI texture metrics*		
TCH	0.480	**	B3 mean (5 × 5)	-0.396	*
MeanCH	0.614	**	B3 mean (7 × 7)	-0.394	*
MedCH	0.595	**	B3 mean (9 × 9)	-0.395	*
h_{60}	0.583	**	B3 mean (11 × 11)	-0.397	*
h_{70}	0.575	**	B4 variance (3 × 3)	0.482	**
h_{80}	0.573	**	B4 variance (5 × 5)	0.508	**
h_{90}	0.573	**	B4 variance (7 × 7)	0.506	**
			B4 homogeneity (5 × 5)	-0.506	**
LiDAR LP variables			B4 homogeneity (3 × 3)	0.519	**
LP1	-0.468	**	B4 homogeneity (7 × 7)	-0.516	**
LP2	-0.411	*	B4 homogeneity (9 × 9)	-0.516	**
LP5	-0.441	*	B4 homogeneity (11 × 11)	-0.512	**

LP7	-0.540	**	B5 homogeneity (3 × 3)	0.366	*
LP10	-0.610	**	B4 contrast (3 × 3)	0.510	**
LP12	-0.677	**	B4 contrast (5 × 5)	0.506	**
LP14	-0.734	**	B4 contrast (7 × 7)	0.516	**
LP16	-0.766	**	B4 contrast (9 × 9)	0.516	**
LP18	-0.779	**	B4 contrast (11 × 11)	0.512	**
LP20	-0.786	**	B4 dissimilarity (3 × 3)	0.510	**
LP24	-0.790	**	B4 dissimilarity (5 × 5)	0.506	**
LP28	-0.760	**	B4 dissimilarity (9 × 9)	0.516	**
			B4 dissimilarity (11 × 11)	0.512	**
Landsat 8 OLI vegetation indices			B4 entrophy (3 × 3)	0.510	**
NDVI	0.406	*	B4 entrophy (7 × 7)	0.510	**
TVI	0.406	*	B4 entrophy (5 × 5)	0.506	**
SVI	-0.419	*	B4 entrophy (9 × 9)	0.512	**
RVI	0.411	*	B4 entrophy (11 × 11)	0.512	**
NRVI	0.418	*	B5 entrophy (3 × 3)	0.429	*
SAVI	0.417	*	B5 entrophy (7 × 7)	0.426	*
			B5 entrophy (5 × 5)	0.424	*
			B5 entrophy (9 × 9)	0.420	*
			B5 entrophy (11 × 11)	0.409	*
			B4 second moment (3 × 3)	-0.510	**
			B4 second moment (5 × 5)	-0.411	*
			B4 second moment (7 × 7)	-0.511	**
			B4 second moment (9 × 9)	-0.513	**
			B4 second moment (11 × 11)	-0.513	**
			B5 second moment (3 × 3)	-0.425	*
			B5 second moment (7 × 7)	-0.422	*
			B5 second moment (9 × 9)	-0.416	*
			B5 second moment (11 × 11)	-0.406	*
			B4 correlation (7 × 7)	-0.515	**
			B4 correlation (9 × 9)	-0.505	**
			B4 correlation (11 × 11)	-0.503	**
			B5 correlation (3 × 3)	-0.406	*
			B5 correlation (5 × 5)	-0.516	**

**Significant at the 0.01 level.

*Significant at the 0.05 level.

3.2 Models by multiple regression analysis

The results of stepwise multiple regression analysis for the AGB estimation is shown in Table 4. When only the variables from Landsat 8 OLI image were used in the regression analysis, the best model included two LiDAR variables and two texture variables (Table 4a and Fig. 2a). The model had an R^2_{adj} of 0.52 and an RMSE of 156.45 t/ha, corresponding to 24.22% of the mean AGB. The texture variable of correlation of band 4 (red) with 3 × 3 moving window contributed the most to this model, followed by correlation of band 5 (near-Infrared) with 5 × 5 moving window, and homogeneity of band 5 (near-Infrared) with 5 × 5 moving window. When only LiDAR variables were used in the regression analysis, the best model selected a single laser penetration variable, LP24, and produced an R^2_{adj} of 0.63 and an RMSE of 163.11 t/ha, corresponding to 25.25% of the mean AGB (Table 4a and Fig. 2b).

Table 4a

Results of multiple regression analysis of airborne LiDAR data, Landsat 8 OLI image and a combination use of airborne LiDAR and Landsat 8 OLI image.

Data type	Dependent variable	Independent variables	Adjusted R^2	RMSE (t/ha)	RMSEcv (t/ha)	Mean prediction bias (t/ha)[1]
LiDAR	ln(AGB)	lnLP24	0.63	163.11 (25.25%)	178.77 (27.67%)	13.36
Landsat 8 OLI	AGB	B4 correlation (3x3) B5 correlation (5x5) B5 homogeneity (5x5)	0.52	156.45 (24.22%)	191.19 (29.59%)	4.24

Combined LiDAR and Landsat 8 OLI	ln(AGB)	lnLP24 B3 mean (3x3) lnMedCH B3 second moment (5x5)	0.81	112.15 (17.36%)	131.33 (20.33%)	7.01

Table 4b

Stepwise regression results for the best model

Model	Unstandardized Coefficients		Standardized Coefficients	t	Sig.	Collinearity Statistics	
	B	Std. Error	Beta			Tolerance	VIF
(Constant)	2.015	1.168	–	1.725	0.097	–	–
lnLP24	-0.692	0.131	-0.602	-5.275	0	0.496	2.017
mean 3x3 _b3	-0.309	0.081	-0.311	-3.842	0.001	0.988	1.012
ln_mediandchm	0.517	0.154	0.392	3.368	0.002	0.476	2.1
Second moment 5x5 _b3	2.708	0.967	0.241	2.8	0.01	0.87	1.149

For the combined use of the variables from airborne LiDAR and Landsat 8 OLI data, we obtained an improved model with two LiDAR variable and two Landsat 8 OLI variables in which both of them were texture variables (Table 4a and Fig. 2c). The model yielded a higher R^2_{adj} value at 0.81 and a lower RMSE at 112.15 t/ha, corresponding to 17.36% of the mean AGB compared to the models with only Landsat 8 OLI or LiDAR variables. The laser penetration variable LP24 contributed the most to this model, followed by the mean of band 3 (green) with 3 × 3 moving window, the MedCH of LiDAR height variable and the second moment of band 3 (green) with 5 × 5 window.

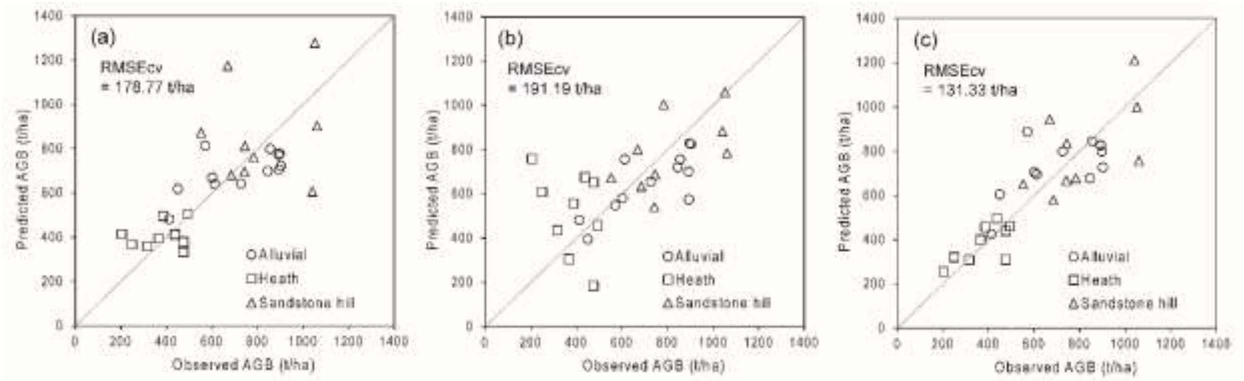

Fig. 2. Observed AGB (t/ha) versus estimated AGB (t/ha). Using variables derived from (a) airborne LiDAR, (b) Landsat 8 OLI, (c) airborne LiDAR and Landsat 8 OLI. The estimated AGB values were from the leave-one-out cross validation.

4. Discussion

In this study, we investigated the performance of variables derived from Landsat 8 OLI sensor with airborne LiDAR metrics to estimate AGB in tropical lowland rainforests. The results from this study showed that texture measures calculated from Landsat 8 OLI images, such as homogeneity, correlation, second moment and mean were more effective than spectral vegetation indices. While 41 texture measures were significantly correlated with AGB, none of the variables from the tasseled cap transformation and vegetation index showed significant correlations with AGB. Similar observations were reported in previous researches using Landsat data (Lu 2005; Kelsey and Neff 2014; Dube and Mutanga 2015a). Vegetation indices are not likely to perform well in the closed canopy forests with complex structure because of 1) saturation problems and 2) shadow effects of the tall trees (Lu et al., 2004; Dube et al. 2014). These explain why the vegetation indices had low correlations with AGB in the SFR forests.

On the other hand, textures measures from Landsat 8 OLI image exhibit greater potential for AGB estimation. Texture measures have the capability to enhance the discrimination of spatial information and AGB detection levels simultaneously which could not be measured with spectral vegetation indices (Eckert, 2012; Santos et al., 2003; Sarker and Nichol, 2011; Vashum and Jayakumar, 2012; Xu et al., 2011). Texture measures from medium-to-high spatial resolution images are also capable of simplifying complex canopy structure information and have strong correlation with forest stand structure including density, age, and leaf area index (Champion et al., 2008; Barbosa et al., 2014; Eckert, 2012). Several studies pointed out that the texture measures were sensitive to the spatial aspects of canopy shadow (Eckert, 2012; Sarker and Nichol, 2011). Among the three forest types of this study (alluvial, heath and sandstone hill forests), the alluvial and sandstone hill forests which store greater AGB generally have larger crown sizes compared to the heath forest which has smaller AGB (Table 1b). The plots in these two forests are dominated by a few large trees with large crown diameters that create a substantial shadowing effect (Table 1a and 1b). In contrast, the plots in the heath forest have a much higher number of stems with relatively small crown sizes. These differences lead to higher canopy ruggedness in the Landsat OLI image for alluvial and sandstone hill forests, whereas in the heath forest, the canopy texture is relatively smooth. This shadowing effect is further enhanced by the greater variability in over-story canopy heights in these two forests. In combination, these differences contributed to the value of the texture measures that correlated to AGB such as correlation and second moment (Table 4b). For the best model, 63% of the AGB variance was explained by the laser penetration variable at 24 m, and the remaining 18% contributed by band 3 mean (3 × 3), lnMedCH and band 3 second moment (5 × 5). The only texture measure retained in the best model was band 3 second moment, and this captured the relatively high orderliness of the pixel values in the heath forest (approaching a value of 1), but less so for the more heterogeneous alluvial and sandstone hill forests.

The window sizes for the selected texture variables were much larger (0.81 ha and 2.25 ha for 3 × 3 and 5 × 5 window sizes) than the plot sizes used in this study (0.09 ha and 0.25 ha).

This mismatch in spatial scales between field inventory plots and larger pixels of images has the potential to introduce errors, especially if forest AGB shows strong local spatial variation (Réjou-Méchain et al. 2014). Whether this is an issue in our study is unknown and it should be examined in future studies

The good performance of texture measures in the AGB modeling can be attributed to the sensor's design of Landsat 8 OLI. The push-broom sensor design of Landsat 8 OLI receives stronger signals and has improved signal-to-noise performance due to its long and linear arrays of detectors (Irons et al. 2012). The spectral range of Landsat 8 OLI is also narrower and the refinement of OLI bands could help avoid atmospheric absorption feature (Lu 2006; Irons et al. 2012; Li et al. 2013). These technical improvements allow accurate surface spectral detection and reduce spectral saturation problems (Dube and Mutanga 2015a).

LiDAR variables, especially the laser penetration variables, had better correlation with AGB than most of the texture measures. The highest *r* was observed for LP24 (-0.790), followed by LP20 (-0.786). The strong correlations between the LP variables and the AGB are most likely related to the canopy height differences of the three different forest types. Stepwise multiple regression analysis showed that a single variable (LP24) was sufficient for AGB prediction. The Lorey's mean height of the alluvial forest, the heath forest, and the sandstone hill forest are 43.27 m, 24.09 m and 35.12 m respectively. This suggests that most of the tree canopies were located above 18 – 20 m in the alluvial and sandstone forests which had the greatest amount of AGB. Therefore, lower penetration rates were observed at heights below 24 m after the lasers travelled through the canopies in these forests. The heath forest had higher penetration rates at 20 m and above because most of the canopies were located only at around 20 – 25 m height. LP variables have explained the AGB difference between the forests with relatively large AGB (alluvial and sandstone hill forests) and the heath forest where smaller AGB was stored. In other literatures, variables derived directly from the LiDAR height statistics are often selected as the

AGB predictor in tropical forests (Asner et al. 2012a; Ota et al. 2015). However, in this study, LP variables were the better predictors for AGB, because LP variables are probably linked to the canopy structure difference of forest types (Ioki et al. 2016). Our result indicates the potential use of LP variables for AGB estimation in primary tropical forests with different forest types.

The combination of Landsat 8 OLI image and airborne LiDAR data further improved the accuracy of AGB estimation, compared to when these two data were separately used (R^2_{adj} increased from 0.52 and 0.63 respectively, to 0.81), suggesting complementarity of these data. Combinations of LiDAR and hyperspectral/high-resolution multi-spectral data, and combinations of Landsat and SAR images have been explored previously (Popescu et al. 2004; Swatantran et al. 2011; Laurin et al. 2014; Cutler et al. 2012), we know of only one previous study that combined LiDAR and Landsat data to estimate AGB (Hyde et al. 2006). Hyde et al. (2006) examined the combination use of multi-sensors (LiDAR, SAR/InSAR, ETM+, Quickbird) for estimating AGB in the Sierra Nevada Mountains of California, USA. In their study, the combination use of Landsat ETM+ image and airborne LiDAR data produced the best regression model. The sensor improvement of Landsat 8 OLI will provide better opportunities for the integrated use with airborne LiDAR data in AGB estimation. To determine the applicability of our approach, further research should be carried out in other tropical forest types or over larger scales.

5. Conclusion

This study examined AGB estimation using Landsat 8 OLI image, airborne LiDAR data, and the combination of both in SFR, Malaysia, where three distinctive forest types exist. The research can be summarized as follows:

- A number of significant correlations were observed between texture measures from Landsat 8 OLI image and field observed AGB. Compared with the spectral vegetation index, the texture measures have more potential for estimating AGB of dense tropical rainforests, where there are high possibilities of saturation problems.
- The laser penetration variables from airborne LiDAR data performed well in the prediction of AGB. These variables detected differences in canopy structures in the three distinctive forest types studied.
- When the variables from Landsat 8 OLI images and airborne LiDAR data were integrated in the regression model, the estimation accuracy of AGB was improved. The combined use of airborne LiDAR data and Landsat 8 OLI image for estimating AGB of an old growth tropical rainforest appeared promising.

While airborne LiDAR data acquisition is currently too expensive for large spatial scale applications, the deployment of spaceborne LiDAR will lead to potential global application of LiDAR data. In the near future, together with the technological improvement, more remote sensing data (e.g., new spaceborne LiDAR data) will be widely available. The synergistic use of these remote sensing data deserves intensified attention in future research on AGB estimation in the tropics.

Acknowledgements

We sincerely thank Sabah Forestry Department for the research permission and Sabah Forest Industry (SFI) for the field support. We also thank Dr. Nobuyuki Imai of Tokyo University of Agriculture for ecological interpretation of the field data. This work was supported by the Ministry of Higher Education of Malaysia [grant number RACE0004-STW-2012].

References

Asner, G. P., Clark, J. K., Mascaro, J., Vaudry, R., Chadwick, K. D., Vieilledent, G., Rosamoelina, M., Balaji, A., Kennedy-Bowdoin, T., Maatoug, L., Colgan, M. S., & Knapp, D.E. (2012a). Human and environmental controls over aboveground carbon storage in Madagascar. Carbon Balance And Management, 7(1), 2.

Asner, G. P., Mascaro, J., Muller-Landau, H. C., Vieilledent, G., Vaudry, R., Rasamoelina, M., Hall, J.F., & Van Breugel, M. (2012b). A universal airborne LiDAR approach for tropical forest carbon mapping. Oecologia, 168(4), 1147-1160.

Asner, G. P, Powell, G. V. N., Mascaro, J., Knapp, D. E., Clark, J. K., Jacobson, J., Kennedy-Bowdoin, T., Balaji, A., Paez-Acosta, G., Victoria, E., Secada, L., Valqui, M., & Hughes, R. F. (2010). High-resolution forest carbon stocks and emissions in the Amazon. Proceedings of the National Academy of Sciences USA 107:16738-16742.

Baker, T. R., Phillips, O. L., Malhi, Y., Almeida, S., Arroyo, L., Di Fiore, A., Erwin, T., Killeen, T.J., Laurance, S.G., Laurance, W.F., Lewis, S. L., Lloyd, J., Monteagudo, A., Neill, D.A., Patino, S., Pitman, N.C.A., Silva, N.M., & Martinez, R.V. (2004). Variation in wood density determines spatial patterns in Amazonian forest biomass. Global Change Biology, 10(5), 545-562.

Balzter, H., Rowland, C. S., & Saich, P. (2007). Forest canopy height and carbon estimation at Monks Wood National Nature Reserve, UK, using dual-wavelength SAR interferometry. Remote Sensing of Environment, 108(3), 224-239.

Barbosa, J. M., Broadbent, E. N., & Bitencourt, M. D. (2014). Remote sensing of aboveground biomass in tropical secondary forests: a review. International Journal of Forestry Research, 2014.

Basuki, T. M., Van Laake, P. E., Skidmore, A. K., & Hussin, Y. A. (2009). Allometric equations for estimating the above-ground biomass in tropical lowland Dipterocarp forests. Forest Ecology and Management, 257(8), 1684-1694.

Brown, S., & Lugo, A. E. (1982). The storage and production of organic matter in tropical forests and their role in the global carbon cycle. Biotropica, 161-187.

Brown, S. (2002). Measuring carbon in forests: current status and future challenges. Environmental pollution, 116(3), 363-372.

Champion, I., Dubois-Fernandez, P., Guyon, D., & Cottrel, M. (2008). Radar image texture as a function of forest stand age. International Journal of Remote Sensing, 29(6), 1795-1800.

Chave, J., Andalo, C., Brown, S., Cairns, M. A., Chambers, J. Q., Eamus, D., Folster, H., Fromard, F., Higuchi, N., Kira, T., Lescure, J. P., Nelson, B.W., Ogawa, H., Puig, H., Riera, B., & Yamakura, T. (2005). Tree allometry and improved estimation of carbon stocks and balance in tropical forests. Oecologia, 145(1), 87-99.

Chavez, P. S. (1988). An improved dark-object subtraction technique for atmospheric scattering correction of multispectral data. Remote Sensing of Environment, 24(3), 459-479.

Cutler, M. E. J., Boyd, D. S., Foody, G. M., & Vetrivel, A. (2012). Estimating tropical forest biomass with a combination of SAR image texture and Landsat TM data: An assessment of predictions between regions. ISPRS Journal of Photogrammetry and Remote Sensing, 70, 66-77.

Dalponte, M., & Coomes, D. A. (2016). Tree-centric mapping of forest carbon density from airborne laser scanning and hyperspectral data. Methods in Ecology and Evolution 7 (10), 1236-1245)

Drake, J. B., Knox, R. G., Dubayah, R. O., Clark, D. B., Condit, R., Blair, J. B., & Hofton, M. (2003). Above-ground biomass estimation in closed canopy neotropical forests using lidar remote sensing: Factors affecting the generality of relationships. Global Ecology and Biogeography, 12(2), 147-159.

Dube, T., & Mutanga, O. (2015a). Investigating the robustness of the new Landsat-8 Operational Land Imager derived texture metrics in estimating plantation forest aboveground biomass in resource constrained areas. ISPRS Journal of Photogrammetry and Remote Sensing, 108, 12-32.

Dube, T., & Mutanga, O. (2015b). Evaluating the utility of the medium-spatial resolution Landsat 8 multispectral sensor in quantifying aboveground biomass in uMgeni catchment, South Africa. ISPRS Journal of Photogrammetry and Remote Sensing, 101, 36-46.

Dube, T., Mutanga, O., Elhadi, A., & Ismail, R. (2014). Intra-and-inter species biomass prediction in a plantation forest: testing the utility of high spatial resolution spaceborne multispectral rapideye sensor and advanced machine learning algorithms. Sensors, 14(8), 15348-15370.

Eckert, S. (2012). Improved forest biomass and carbon estimations using texture measures from WorldView-2 satellite data. Remote sensing, 4(4), 810-829.

Englhart, S., Keuck, V., & Siegert, F. (2011). Aboveground biomass retrieval in tropical forests-the potential of combined X-and L-band SAR data use. Remote Sensing of Environment, 115(5), 1260-1271.

Foody, G. M., Boyd, D. S., & Cutler, M. E. (2003). Predictive relations of tropical forest biomass from Landsat TM data and their transferability between regions. Remote Sensing of Environment, 85(4), 463-474.

Foody, G. M., Cutler, M. E., Mcmorrow, J., Pelz, D., Tangki, H., Boyd, D. S., & Douglas, I. (2001). Mapping the biomass of Bornean tropical rain forest from remotely sensed data. Global Ecology and Biogeography, 10(4), 379-387.

Fox, J.E.D. (1973). A Handbook to Kabili-Sepilok Forest Reserve, Sabah Forest Record No. 9. Borneo Literature Bureau, Kuching, Sarawak, Malaysia.

Gibbs, H. K., Brown, S., Niles, J. O., & Foley, J. A. (2007). Monitoring and estimating tropical forest carbon stocks: making REDD a reality. Environmental Research Letters, 2(4), 045023.

Hall, R. J., Skakun, R. S., Arsenault, E. J., & Case, B. S. (2006). Modeling forest stand structure attributes using Landsat ETM+ data: Application to mapping of aboveground biomass and stand volume. Forest Ecology and Management, 225(1), 378-390.

Haralick, R. M., & Shanmugam, K., & Dinstein, I. (1973). Textural features for image classification. IEEE Transactions on Systems, Man, and Cybernetics, 3(6), 610-621.

Houghton, R. A., Lawrence, K. T., Hackler, J. L., & Brown, S. (2001). The spatial distribution of forest biomass in the Brazilian Amazon: a comparison of estimates. Global Change Biology, 7(7), 731-746.

Huston, M. A., & Marland, G. (2003). Carbon management and biodiversity. Journal of Environmental Management, 67(1), 77-86.

Hyde, P., Dubayah, R., Walker, W., Blair, J. B., Hofton, M., & Hunsaker, C. (2006). Mapping forest structure for wildlife habitat analysis using multi-sensor (LiDAR, SAR/InSAR, ETM+, Quickbird) synergy. Remote Sensing of Environment, 102(1), 63-73.

Imai N, Tanaka A, Samejima H, Sugau JB, Pereira JT, Titin J, Kurniawan Y, & Kitayama K (2014). Tree community composition as an indicator in biodiversity monitoring of REDD+. Forest Ecology and Management 313: 169-179.

Ingram, J. C., Dawson, T. P., & Whittaker, R. J. (2005). Mapping tropical forest structure in southeastern Madagascar using remote sensing and artificial neural networks. Remote Sensing of Environment, 94(4), 491-507.

Ioki, K., Tsuyuki, S., Hirata, Y., Phua, M. -H., Wong, W.V.C., Ling, Z. -Y., Saito, H., & Takao, G. (2014). Estimating above-ground biomass of tropical rainforest of different degradation levels in Northern Borneo using airborne LiDAR. Forest Ecology and Management, 328, 335-341.

Ioki, K., Tsuyuki, S., Hirata, Y., Phua, M. H., Wong, W. V. C., Ling, Z. Y., Johari, S. A., Korom, A., James, D., Saito, H., & Takao, G. (2016). Evaluation of the similarity in tree community composition in a tropical rainforest using airborne LiDAR data. Remote Sensing of Environment, 173, 304-313.

Irons, J. R., Dwyer, J. L., & Barsi, J. A. (2012). The next Landsat satellite: The Landsat data continuity mission. Remote Sensing of Environment, 122, 11-21.

Karlson, M., Ostwald, M., Reese, H., Sanou, J., Tankoano, B., & Mattsson, E. (2015). Mapping tree canopy cover and aboveground biomass in Sudano-Sahelian woodlands using Landsat 8 and random forest. Remote Sensing, 7(8), 10017-10041.

Kelsey, K. C., & Neff, J. C. (2014). Estimates of aboveground biomass from texture analysis of Landsat imagery. Remote Sensing, 6(7), 6407-6422.

Köhler, P., & Huth, A. (2010). Towards ground-truthing of spaceborne estimates of above-ground life biomass and leaf area index in tropical rain forests. Biogeosciences, 7, 2531-2543.

Krieger, G., Moreira, A., Fiedler, H., Hajnsek, I., Werner, M., Younis, M., & Zink, M. (2007). TanDEM-X: A satellite formation for high-resolution SAR interferometry. IEEE Transactions on Geoscience and Remote Sensing, 45(11), 3317-3341.

Kugler, F., Schulze, D., Hajnsek, I., Pretzsch, H., & Papathanassiou, K. P. (2014). TanDEM-X Pol-InSAR performance for forest height estimation. IEEE Transactions on Geoscience and Remote Sensing, 52(10), 6404-6422.

Koch, B. (2010). Status and future of laser scanning, synthetic aperture radar and hyperspectral remote sensing data for forest biomass assessment. ISPRS Journal of Photogrammetry and Remote Sensing, 65(6), 581-590.

Laurin, G. V., Chen, Q., Lindsell, J. A., Coomes, D. A., Del Frate, F., Guerriero, L., Pirotti, F., & Valentini, R. (2014). Above ground biomass estimation in an African tropical forest with lidar and hyperspectral data. ISPRS Journal of Photogrammetry and Remote Sensing, 89, 49-58.

Lemmens, R. H. M. J., Soerianegara, I., & Wong, W. C. (1995). Timber trees: minor commercial timbers. Prosea Foundation, Bogor, Indonesia.

Li, P., Jiang, L., & Feng, Z. (2013). Cross-comparison of vegetation indices derived from Landsat-7 enhanced thematic mapper plus (ETM+) and Landsat-8 operational land imager (OLI) sensors. Remote Sensing, 6(1), 310-329.

Lu, D. (2005). Aboveground biomass estimation using Landsat TM data in the Brazilian Amazon. International Journal of Remote Sensing, 26(12), 2509-2525.

Lu, D. (2006). The potential and challenge of remote sensing-based biomass estimation. International Journal of Remote Sensing, 27(7), 1297-1328.

Lu, D., Mausel, P., Brondızio, E., & Moran, E. (2004). Relationships between forest stand parameters and Landsat TM spectral responses in the Brazilian Amazon Basin. Forest Ecology and Management, 198(1), 149-167.

Minh, D. H. T., Le Toan, T., Rocca, F., Tebaldini, S., Villard, L., Réjou-Méchain, M., ... & Chave, J. (2016). SAR tomography for the retrieval of forest biomass and height: Cross-validation at two tropical forest sites in French Guiana. Remote Sensing of Environment, 175, 138-147.

Mitchard, E. T. A., Saatchi, S. S., Lewis, S. L., Feldpausch, T. R., Woodhouse, I. H., Sonké, B., & Meir, P. (2011). Measuring biomass changes due to woody encroachment and deforestation/degradation in a forest–savanna boundary region of central Africa using multi-temporal L-band radar backscatter. Remote Sensing of Environment, 115(11), 2861-2873.

Mitchard, E. T., Saatchi, S. S., Woodhouse, I. H., Nangendo, G., Ribeiro, N. S., Williams, M., Ryan, C. M., Lewis, S. L., Feldpausch, T. R., & Meir, P. (2009). Using satellite radar backscatter to predict above-ground woody biomass: A consistent relationship across four different African landscapes. Geophysical Research Letters, 36(23).

Morel, A. C., Saatchi, S. S., Malhi, Y., Berry, N. J., Banin, L., Burslem, D., Nilus, R., & Ong, R. C. (2011). Estimating aboveground biomass in forest and oil palm plantation in Sabah, Malaysian Borneo using ALOS PALSAR data. Forest Ecology and Management, 262(9), 1786-1798.

Mutanga, O., & Skidmore, A. K. (2004). Narrow band vegetation indices overcome the saturation problem in biomass estimation. International Journal of Remote Sensing, 25(19), 3999-4014.

Mutanga, O., Adam, E., & Cho, M. A. (2012). High density biomass estimation for wetland vegetation using WorldView-2 imagery and random forest regression algorithm. International Journal of Applied Earth Observation and Geoinformation, 18, 399-406.

Nelson, R. F., Kimes, D. S., Salas, W. A., & Routhier, M. (2000a). Secondary Forest Age and Tropical Forest Biomass Estimation Using Thematic Mapper Imagery Single-year tropical forest age classes, a surrogate for standing biomass, cannot be reliably identified using single-date tm imagery. Bioscience, 50(5), 419-431.

Nichol, J. E., & Sarker, M. L. R. (2011). Improved biomass estimation using the texture parameters of two high-resolution optical sensors. IEEE Transactions on Geoscience and Remote Sensing, 49(3), 930-948.

Nilus, R., Maycock, C. R., Majalap-Lee, N., & Burslem, D. F. R. P. (2011). Nutrient limitation of tree seedling growth in three soil types found in Sabah. Journal of Tropical Forest Science, 23 (2), pp. 133–142.

Ota, T., Kajisa, T., Mizoue, N., Yoshida, S., Takao, G., Hirata, Y., Furuya, N., Sano, T., Ponce-Hernandez, R., Ahmed, O. S., Sokh, H., Ma, V., Ito, E., Toriyama, J., & Monda, Y. (2015). Estimating aboveground carbon using airborne LiDAR in Cambodian tropical seasonal forests for REDD+ implementation. Journal of Forest Research, 20(6), 484-492.

Pargal, S., Fararoda, R., Rajashekar, G., Balachandran, N., Réjou-Méchain, M., Barbier, N., ... & Couteron, P. (2017). Inverting Aboveground Biomass–Canopy Texture Relationships in a Landscape of Forest Mosaic in the Western Ghats of India Using Very High Resolution Cartosat Imagery. Remote Sensing, 9(3), 228.

Pandey, U., Kushwaha, S. P. S., Kachhwaha, T. S., Kunwar, P., & Dadhwal, V. K. (2010). Potential of Envisat ASAR data for woody biomass assessment. Tropical Ecology, 51(1), 117.

Phua, M. H., & Saito, H. (2003). Estimation of biomass of a mountainous tropical forest using Landsat TM data. Canadian Journal of Remote Sensing, 29(4), 429-440.

Phua, M. H., Hue, S. W., Ioki, K., Hashim, M., Bidin, K., Musta, B., Suleiman, M., Yap, S. W., & Maycock, C. R. (2016). Estimating Logged-Over Lowland Rainforest Aboveground Biomass in Sabah, Malaysia Using Airborne LiDAR Data. Terrestrial, Atmospheric and Oceanic Sciences, 27(4), 481-489.

Pinto, N., Simard, M., & Dubayah, R. (2012). Using InSAR coherence to map stand age in a boreal forest. Remote Sensing, 5(1), 42-56.

Ploton, P., Pélissier, R., Proisy, C., Flavenot, T., Barbier, N., Rai, S. N., & Couteron, P. (2012). Assessing aboveground tropical forest biomass using Google Earth canopy images. Ecological Applications, 22(3), 993-1003.

Popescu, S. C., Wynne, R. H., & Scrivani, J. A. (2004). Fusion of small-footprint lidar and multispectral data to estimate plot-level volume and biomass in deciduous and pine forests in Virginia, USA. Forest Science, 50(4), 551-565.

Proisy, C., Couteron, P., & Fromard, F. (2007). Predicting and mapping mangrove biomass from canopy grain analysis using Fourier-based textural ordination of IKONOS images. Remote Sensing of Environment, 109(3), 379-392.

Réjou-Mechain, M., Muller-Landau, H. C., Detto, M., Thomas, S. C., Le Toan, T., Saatchi, S. S., ... & Brockelman, W. Y. (2014). Local spatial structure of forest biomass and its consequences for remote sensing of carbon stocks. Biogeosciences, 11(23), 6827-6840.

Roy, P. S., & Ravan, S. A. (1996). Biomass estimation using satellite remote sensing data—an investigation on possible approaches for natural forest. Journal of Biosciences, 21(4), 535-561.

Saatchi, S., Marlier, M., Chazdon, R. L., Clark, D. B., & Russell, A. E. (2011). Impact of spatial variability of tropical forest structure on radar estimation of aboveground biomass. Remote Sensing of Environment, 115(11), 2836-2849.

Sader, S. A., Waide, R. B., Lawrence, W. T., & Joyce, A. T. (1989). Tropical forest biomass and successional age class relationships to a vegetation index derived from Landsat TM data. Remote Sensing of Environment, 28, 143-156.

Santos, J. R., Freitas, C. C., Araujo, L. S., Dutra, L. V., Mura, J. C., Gama, F. F., Soler, L. S., & Sant'Anna, S. J. S. (2003). Airborne P-band SAR applied to the aboveground biomass studies in the Brazilian tropical rainforest. Remote Sensing of Environment, 87(4), 482-493.

Sarker, L. R., & Nichol, J. E. (2011). Improved forest biomass estimates using ALOS AVNIR-2 texture indices. Remote Sensing of Environment, 115(4), 968-977.

Slik, J. W. F. (2006). Estimating species-specific wood density from the genus average in Indonesian trees. Journal of Tropical Ecology, 22(04), 481-482.

Soerianegara, I., & Lemmens, R. H. M. J. (1993). Timber trees: major commercial timbers. Pudoc Scientific Publishers, Wageningen, The Netherlands.

Sosef, M. S. M., Hong, L. T., & Prawirohatmodjo, S. (1998). Timber trees: Lesser-known timbers. Prosea Foundation, Bogor, Indonesia.

Stern, N. (2007). The Economics of Climate Change: The Stern Review. Cambridge University Press, Cambridge, pp. 712.

Swatantran, A., Dubayah, R., Roberts, D., Hofton, M., & Blair, J. B. (2011). Mapping biomass and stress in the Sierra Nevada using lidar and hyperspectral data fusion. Remote Sensing of Environment, 115(11), 2917-2930.

Takahashi, T., Awaya, Y., Hirata, Y., Furuya, N., Sakai, T., & Sakai, A. (2010). Stand volume estimation by combining low laser-sampling density LiDAR data with QuickBird panchromatic imagery in closed-canopy Japanese cedar (Cryptomeria japonica) plantations. International Journal of Remote Sensing, 31(5), 1281-1301.

Vashum, K. T., & Jayakumar, S. (2012). Methods to estimate above-ground biomass and carbon stock in natural forests-a review. Journal of Ecosystem and Ecography, 2(4), 1-7.

Wijaya, A., Kusnadi, S., Gloaguen, R., & Heilmeier, H. (2010). Improved strategy for estimating stem volume and forest biomass using moderate resolution remote sensing data and GIS. Journal of Forestry Research, 21(1), 1-12.

Xu, X., Du, H., Zhou, G., Ge, H., Shi, Y., Zhou, Y., Fan, W., & Fan, W. (2011). Estimation of aboveground carbon stock of Moso bamboo (Phyllostachys heterocycla var. pubescens) forest with a Landsat Thematic Mapper image. International Journal of Remote Sensing, 32(5), 1431-1448.

Yamakura, T., Hagihara, A., Sukardjo, S., & Ogawa, H. (1986). Aboveground biomass of tropical rain forest stands in Indonesian Borneo. Vegetatio, 68(2), 71-82.

Zhao, K., Popescu, S., & Nelson, R. (2009). Lidar remote sensing of forest biomass: A scale-invariant estimation approach using airborne lasers. Remote Sensing of Environment, 113(1), 182-196.

Zuur, A.F., Ieno, E. N., & Elphick, C. S. (2010). A protocol for data exploration to avoid common statistical problems. Methods in Ecology and Evolution 1 (1), 3-14.